

# Electronic structure, magnetic properties, and pairing tendencies of the copper-based honeycomb lattice $\text{Na}_2\text{Cu}_2\text{TeO}_6$

Ling-Fang Lin<sup>1</sup>, Rahul Soni<sup>1,2</sup>, Yang Zhang<sup>1</sup>, Shang Gao<sup>2,3</sup>, Adriana Moreo<sup>1,2</sup>, Gonzalo Alvarez,<sup>4</sup> Andrew D. Christianson,<sup>2</sup> Matthew B. Stone<sup>3</sup>, and Elbio Dagotto<sup>1,2</sup>

<sup>1</sup>*Department of Physics and Astronomy, University of Tennessee, Knoxville, Tennessee 37996, USA*

<sup>2</sup>*Materials Science and Technology Division, Oak Ridge National Laboratory, Oak Ridge, Tennessee 37831, USA*

<sup>3</sup>*Neutron Scattering Division, Oak Ridge National Laboratory, Oak Ridge, Tennessee 37831, USA*

<sup>4</sup>*Computational Sciences & Engineering Division, Oak Ridge National Laboratory, Oak Ridge, Tennessee 37831, USA*



(Received 27 March 2022; revised 17 May 2022; accepted 31 May 2022; published 10 June 2022)

Spin-1/2 chains with alternating antiferromagnetic (AFM) and ferromagnetic (FM) couplings have attracted considerable interest due to the topological character of their spin excitations. Here, using density functional theory and density-matrix renormalization-group (DMRG) methods, we have systematically studied the dimerized chain system  $\text{Na}_2\text{Cu}_2\text{TeO}_6$  with a  $d^9$  electronic configuration. Near the Fermi level, in the nonmagnetic phase the dominant states are mainly contributed by the Cu  $3d_{x^2-y^2}$  orbitals highly hybridized with the O  $2p$  orbitals, leading to an “effective” single-orbital low-energy model. By calculating the relevant hopping amplitudes, we explain the size and sign of the exchange interactions in  $\text{Na}_2\text{Cu}_2\text{TeO}_6$ . In addition, a single-orbital Hubbard model is constructed for this dimerized chain system where the quantum fluctuations are taken into account. Both AFM and FM couplings (leading to an  $\uparrow - \downarrow - \downarrow - \uparrow$  state) along the chain were found in our DMRG and Lanczos calculations, in agreement with density functional theory and neutron-scattering results. The hole pairing binding energy  $\Delta E$  is predicted to be negative at Hubbard  $U \sim 11$  eV, suggesting incipient pairing tendencies.

DOI: [10.1103/PhysRevB.105.245113](https://doi.org/10.1103/PhysRevB.105.245113)

## I. INTRODUCTION

One-dimensional (1D) systems continue to attract considerable interest due to their strong quantum fluctuations as well as their intertwined charge, spin, orbital, and lattice degrees of freedom [1–5]. This leads to unusual physical properties, such as superconductivity in copper or iron ladders [6–12], magnetic block states in iron ladders [13,14], orbital-selective Mott phases in 1D chains and ladders [15–22], excitonic magnets in multiorbital models on chains [23,24] ferroelectricity in  $\text{WOX}_4$  ( $X =$  halogen element) [25], charge-density waves in Ta chains [26,27], superconductivity in doped Haldane chains [28], edge Majorana states in the proximity of superconductivity [29], orbital order in ruthenates [30], ferromagnetism and phase separation in multiorbital  $t$ - $J$  model chains [31], and exotic orbital and magnetic properties in van der Waals chains [32].

As the simplest systems, spin-1/2 chains with alternating antiferromagnetic (AFM) and ferromagnetic (FM) couplings display interesting quantum magnetism and gapped excitations [33,34]. These systems usually do not exhibit long-range order at 0 K where the two AFM spins form a spin dimer, leading to a spin-singlet  $(|\uparrow\downarrow\rangle - |\downarrow\uparrow\rangle)/\sqrt{2}$  ground state [33,35,36]. Furthermore, other unusual properties are local singlet-triplet (triplon) excitations [37,38], a hidden string order protected by  $Z_2 \times Z_2$  global rotations; symmetry [39,40], and symmetry-protected topological states [41]. The resource ground state for measurement-based quantum computation [42] is also proposed in the AFM-FM chain systems.

However, spin-1/2 chains usually display standard staggered AFM couplings due to superexchange Hubbard interactions. To the best of our knowledge, only a few of alternating AFM-FM chains are experimentally realized based on neutron-scattering results, including  $\text{CuNb}_2\text{O}_6$  [43],  $\text{DMACuCl}_3$  [44],  $\text{Na}_3\text{Cu}_2\text{SbO}_6$  [45], and  $\text{BaCu}_2\text{V}_2\text{O}_8$  [46]. Recently, the distorted honeycomb lattice compound  $\text{Na}_2\text{Cu}_2\text{TeO}_6$  was proposed to be a FM-AFM dimerized chain system [47–53]. As shown in Fig. 1,  $\text{Na}_2\text{Cu}_2\text{TeO}_6$  has a monoclinic structure with the space-group  $C2/m$  (No. 12), stacking by alternating  $\text{Cu}_2\text{TeO}_6$  and Na layers along the  $c$  axis. In each  $\text{Cu}_2\text{TeO}_6$  layer, the Cu ions form a distorted honeycomb lattice that is composed of edge-sharing  $\text{CuO}_6$  octahedra as displayed in Fig. 1(b). In this system, the valence of Cu is  $2+$ , leading to an effective  $S = 1/2$  spin of Cu (corresponding to the  $d^9$  electronic configuration). Previous magnetic susceptibility measurements of a powder sample revealed a spin gap  $\Delta \sim 127$  K in this system [47], considered to be related to the strong AFM couplings  $J_1$  [47,49,51].

Very recently, a singlet-triplet excitation was reported in  $\text{Na}_2\text{Cu}_2\text{TeO}_6$  single crystals by inelastic neutron-scattering experiments [52]. Based on neutron experiments [52],  $J_1$  ( $\sim 22.78$  meV) is larger than  $J_2$  ( $\sim -8.73$  meV), although the length between two Cu sites along the  $J_1$  path (5.806 Å) is much longer than the one along the  $J_2$  path (2.850 Å) [see Fig. 1(b)]. Hence, two simple questions naturally arise: why  $\text{Na}_2\text{Cu}_2\text{TeO}_6$  displays FM-AFM couplings along the dimerized chain direction? Why  $J_1$  is much larger than  $J_2$ ?

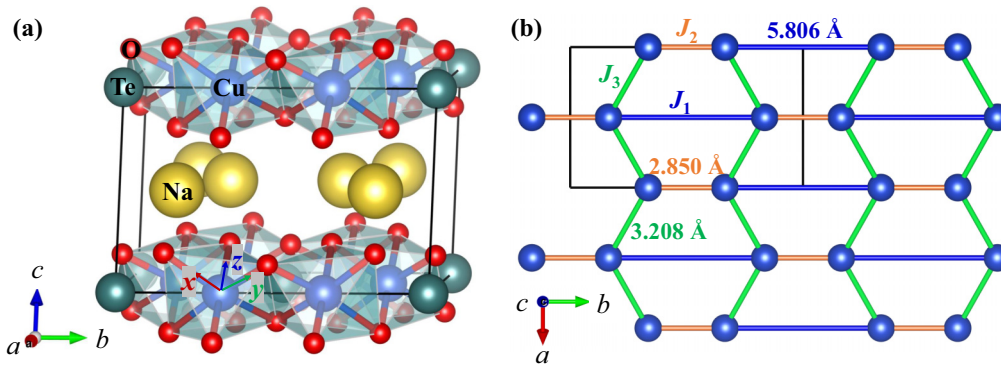


FIG. 1. Schematic crystal structure of  $\text{Na}_2\text{Cu}_2\text{TeO}_6$ : in yellow Na; in blue Cu; in dark cyan Te; in red O. (a) Conventional cell of the bulk structure. (b) Sketch of the Cu single-layer lattice. Different magnetic exchange couplings are shown in different colors. Note that the local  $\{x, y, z\}$  axes are (almost) along the Cu-O bond directions as marked in (a), leading to  $d_{x^2-y^2}$  orbitals spanning over the  $\text{CuO}_4$  plane.

In the dimerized chain direction, the long-distanced Cu-Cu sites form AFM spin dimers but not the short-distanced Cu-Cu sites, indicating that O sites must be playing a key role. Furthermore, the interchain coupling  $J_3$  is considered much smaller than  $J_1$  and  $J_2$ . Considering that superconductivity was widely reported in hole-doped Cu-based compounds with  $d^9$  configuration [2,6,7], is it possible to obtain superconductivity in  $\text{Na}_2\text{Cu}_2\text{TeO}_6$  under hole doping as well?

To answer these questions, we have systematically studied the dimerized chain  $\text{Na}_2\text{Cu}_2\text{TeO}_6$  by using first-principles density functional theory (DFT) and the density-matrix renormalization-group (DMRG) and Lanczos calculations. First, our DFT calculations found that the states near the Fermi level are mainly contributed by Cu  $3d$  states with a small bandwidth, which are highly hybridized with O  $2p$  orbitals in the nonmagnetic (NM) state, leading to an “effective” single-orbital low-energy model. By mapping the DFT energies to the Heisenberg model, we obtained AFM couplings  $J_1$  and  $J_3$  whereas  $J_2$  is FM, in agreement with the previously mentioned results. In addition, we explained the size and sign of the exchange interactions along the dimerized chain direction. Specifically, the strong Cu-O-O-Cu super-super exchange plays the most important role for the largest magnetic coupling. Furthermore, the Cu-O-Cu angle is close to  $90^\circ$ , which leads to the FM character of  $J_2$  because a pair of orthogonal O  $2p$  orbitals with parallel spins are involved in the virtual electron hopping.

In addition, we constructed a single-orbital Hubbard model for the dimerized chain where quantum fluctuations were taken into account. The block AFM-FM state ( $\uparrow - \downarrow - \downarrow - \uparrow$ ) along the chain was found to be the ground state in our DMRG calculations, in agreement with DFT and neutron results. Furthermore, we calculated the binding energy  $\Delta E$  and found it becomes negative for Hubbard  $U \sim 11$  eV, indicating a possible pairing tendency. However, these pairs may be too small to sustain a robust coherent superconductor. Furthermore, we also studied different hole-doping cases, reaching similar conclusions.

## II. DFT METHOD

In the present paper, first-principles calculations, using the projector augmented-wave method, were employed based

on DFT as implemented in the Vienna *ab initio* simulation package code [54–56]. Electronic correlations were considered by using the generalized gradient approximation and the revised Perdew-Burke-Ernzerhof function [57,58]. The plane-wave cutoff energy was set as 550 eV. Furthermore, the  $k$ -point mesh adopted was  $6 \times 4 \times 6$  for the conventional cell of  $\text{Na}_2\text{Cu}_2\text{TeO}_6$ . Note that this  $k$ -point mesh was tested explicitly to verify that it already leads to converged energies. For the magnetic calculations, on-site Coulomb interactions were considered by using the local spin-density approximation (LSDA) plus  $U$  with the Liechtenstein formulation for the double-counting term [59]. In addition to the standard DFT calculation discussed thus far, the maximally localized Wannier functions (MLWFs) method was employed using the WANNIER90 code [60,61] with the functions centered at the Cu’s  $3d_{x^2-y^2}$ . All the crystal structures were visualized with the VESTA code [62].

## III. DFT RESULTS

### A. Electronic properties

First, let us discuss the electronic structures for the NM phase of  $\text{Na}_2\text{Cu}_2\text{TeO}_6$ . Note that the local  $\{x, y, z\}$  axes of the projected orbitals are marked in Fig. 1(a) where the local  $\{x, y, z\}$  axes are (almost) along the Cu-O bond directions, leading to  $d_{x^2-y^2}$  orbitals spanning over the  $\text{CuO}_4$  plane. As shown in Fig. 2(a), the states near the Fermi level are mainly contributed by the Cu  $3d$  orbitals, highly hybridized with the O  $2p$  orbitals.  $\text{Na}_2\text{Cu}_2\text{TeO}_6$  turns out to be a charge-transfer system, similar to the cuprate superconductors [2,63]. Furthermore, the calculated DOS indicates a small gap  $\sim 0.09$  eV for  $\text{Na}_2\text{Cu}_2\text{TeO}_6$ . This small gap is caused by the dimerization of the antibonding  $\sigma$  combination of Cu  $3d_{x^2-y^2}$  and O  $2p$  states in the distorted honeycomb lattice structure.

Next, to better understand the contribution of Cu  $3d$  orbitals, we also calculated the orbital-resolved band structure and DOS. Figures 2(b) and 2(c) show that the  $d_{x^2-y^2}$  band of Cu’s  $3d$  is located near the Fermi level (range  $-0.5$  eV to  $0.3$  eV), whereas other Cu’s  $3d$  orbitals ( $d_{3z^2-r^2}$ ,  $d_{xz}$ ,  $d_{yz}$ , and  $d_{xy}$ ) are fully occupied and at lower energies. In this case, the physical properties of this system are mainly contributed by the  $d_{x^2-y^2}$  orbital, i.e., by considering the Cu  $3d^9$  configuration

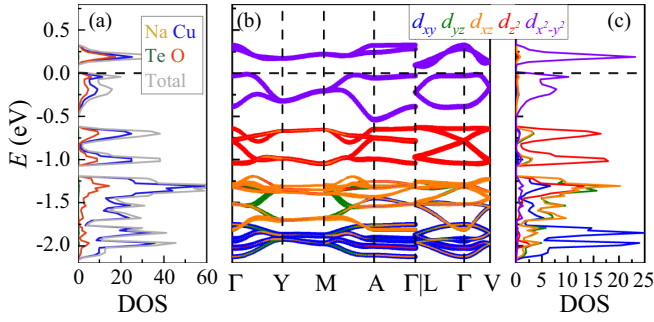


FIG. 2. (a) Density of states (DOS) near the Fermi level of  $\text{Na}_2\text{Cu}_2\text{TeO}_6$  for the NM phase (in gray: total; in yellow: Na; in blue: Cu; in dark cyan: Te; in red: O). (b) Projected band structures and (c) DOS of the NM phase for  $\text{Na}_2\text{Cu}_2\text{TeO}_6$ , respectively. Note that the local  $\{x, y, z\}$  axes of projected orbitals are marked in Fig. 1. The weight of each Cu orbital is represented by the size of the (barely visible) circles for the projected band structures. The coordinates of the high-symmetry points in the bulk Brillouin zone are  $\Gamma = (0, 0, 0)$ ,  $Y = (0.5, 0.5, 0)$ ,  $M = (0.5, 0.5, 0.5)$ ,  $A = (0, 0, 0.5)$ ,  $L = (0, 0.5, 0.5)$ , and  $V = (0, 0.5, 0)$  in units of reciprocal basis vectors.

in  $\text{Na}_2\text{Cu}_2\text{TeO}_6$ . Moreover, the bandwidth  $W$  of  $d_{x^2-y^2}$  is small ( $\sim 0.8$  eV), leading to a strong electronic correlation effect ( $U/W$ ) in this system. Hence, by introducing the Hubbard  $U$ , this system should be a Mott insulator due to the half-filling of the  $d_{x^2-y^2}$  orbital of  $\text{Na}_2\text{Cu}_2\text{TeO}_6$ , as discussed in the following section.

According to the crystal-splitting analysis and electronic structures discussed above, the  $d_{x^2-y^2}$  orbital, located near the Fermi level (range  $\sim -0.5$  to  $\sim 0.3$  eV), determines the physical properties of this system, leading to a single-band low-energy model. To better understand this low-energy model, we constructed one-orbital Wannier functions based on the MLWFs method [60,61], involving a single  $d_{x^2-y^2}$  orbital of Cu's  $3d$  in the NM phase. Figure 3(a) indicates that the single-orbital Wannier band fits very well with the DFT bands. Furthermore, we also plot the effective single orbital Wannier function for one Cu site as shown in Fig. 3(b). It clearly shows an antibonding combination of  $3d_{x^2-y^2}$  and O  $2p \sigma$  states. As a result, this effective single orbital already considers the contribution of O  $2p$  states.

Based on the information calculated from MLWFs, the main hoppings between different Cu-Cu sites are obtained as displayed in Fig. 3(c) where other small hoppings and inter-layer hoppings are excluded for simplicity. Remarkably, in this system the largest hopping is  $t_1 = 0.178$  eV instead of  $t_2$  (the short-distanced Cu-Cu sites), indicating that the Cu-O-O-Cu super-super-exchange interaction plays the key role instead of the direct Cu-Cu magnetic interaction. The largest hopping, involving  $t_1$ , results from the direct overlap of the effective single-orbital Wannier functions (combination of Cu  $3d_{x^2-y^2}$  and O  $2p$  states). This is important for the magnetic spin order as discussed in the next section. The hopping along the  $J_2$  path is significantly smaller ( $t_2 = 0.012$  eV) than  $t_1$  because this hopping originates from the almost orthogonal Wannier functions. In this case, the system forms spin dimers for the long-distanced Cu-Cu sites [see Fig. 3(c)] but not for the short-distanced Cu-Cu sites. Moreover, the interlayer

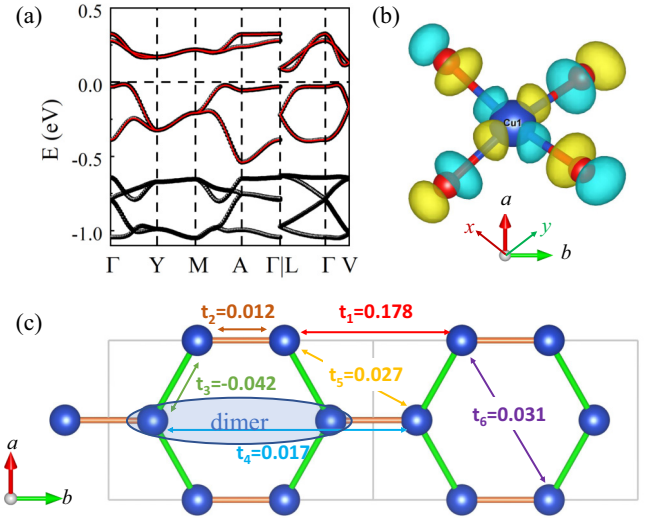


FIG. 3. (a) DFT (in black) and Wannier bands (in red) of the conventional cell of  $\text{Na}_2\text{Cu}_2\text{TeO}_6$ . The Fermi level is shown with dashed horizontal lines. (b) The effective single orbital of the Wannier function for one site; the isosurface is set to 2. Other Wannier functions on other sites have similar properties, not shown here. (c) The relevant hoppings in the intra- $ab$  plane (shown only  $|t| > 0.01$ , in units of eV) based on MLWFs. Note: the interlayer hoppings are quite small ( $\sim 0.014$  eV), and are not shown here.

hoppings are quite small and can be ignored, leading to weak interlayer magnetic coupling. This is physically reasonable because the magnetic properties are mainly contributed by the single half-filled Cu  $3d_{x^2-y^2}$  orbital lying in the  $xy$  plane. Due to its layered crystal structure, the overlap between interlayer Cu  $3d_{x^2-y^2}$  orbitals are expected to be small.

## B. Magnetic properties

To better understand the in-plane magnetic properties of  $\text{Na}_2\text{Cu}_2\text{TeO}_6$ , we also studied several magnetic configurations in plane, including FM, Néel AFM (N-AFM), stripe AFM (S-AFM), zigzag AFM (Z-AFM), and double-stripe AFM (D-AFM) states as shown in Fig. 4. In addition, according to previous experimental results [52] and hopping analysis, the interlayer magnetic coupling should be weak and negligible so that the interlayer magnetic coupling is considered to be FM in our calculation for simplicity. Here, we introduced the electron correlation by using LSDA plus  $U_{\text{eff}}$  ( $U_{\text{eff}} = U - J$ ) with the Dudarev format on Cu sites [64].

By using the  $1 \times 2 \times 1$  supercell of the experimental structure [52], we calculated the energies of various magnetic orders as a function of  $U_{\text{eff}}$  [see Fig. 5(a)]. Note here the  $1 \times 2 \times 1$  supercell is the primitive magnetic unit cell to construct the D-AFM state. The D-AFM state always has the lowest energy among all candidate spin configurations, independent of the choice of  $U_{\text{eff}}$ . Furthermore, the band gaps of different magnetic orders are displayed in Fig. 5(b) where the calculated band gaps are not seriously affected by spin orders. All magnetic-ordered states are insulating and the gaps increase with  $U_{\text{eff}}$  as expected. In addition, the calculated local magnetic moments of Cu of different spin states for different

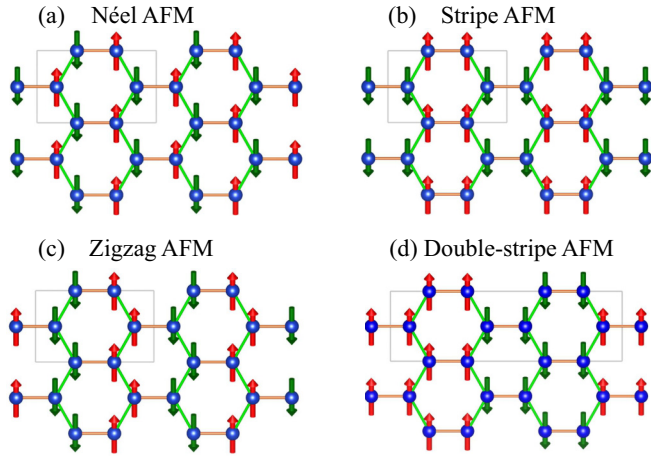


FIG. 4. Sketch of four possible AFM patterns on the plane studied here. Spin up and down are indicated by red and green arrows, respectively.

$U_{\text{eff}}$  are shown in Fig. 5(c), in agreement with an  $S = 1/2$  with  $3d^9$  electronic configuration.

Based on the DFT results, the most important exchange interactions ( $J_1$ ,  $J_2$ , and  $J_3$ ) are estimated by mapping the calculated DFT energies of different AFM states to the Heisenberg model,

$$H = -J_1 \sum_{\langle ij \rangle} \mathbf{S}_i \cdot \mathbf{S}_j - J_2 \sum_{\langle kl \rangle} \mathbf{S}_k \cdot \mathbf{S}_l - J_3 \sum_{\langle mn \rangle} \mathbf{S}_m \cdot \mathbf{S}_n. \quad (1)$$

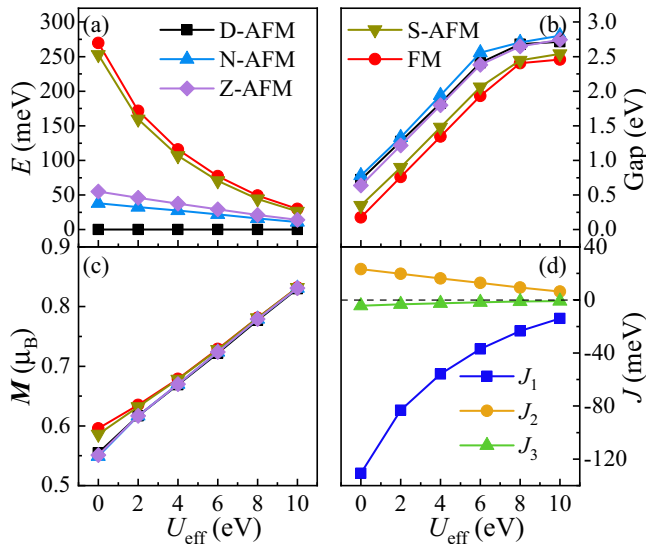


FIG. 5. DFT results for  $\text{Na}_2\text{Cu}_2\text{TeO}_6$  as a function of  $U_{\text{eff}}$ . (a) Energy (total energy of a supercell, including eight Cus) of different spin states. The D-AFM state is taken as the reference. (b) Band gaps of various magnetic orders. (c) Local magnetic moment of Cu calculated within the default Wigner-Seitz sphere. (d) Different magnetic couplings ( $J_1$ ,  $J_2$ , and  $J_3$ ).

where  $J_1/J_2/J_3$  are the in-plane exchange interactions as marked in Fig. 1(b). Four AFM states are used to calculate the spin-exchange parameters,

$$E_{\text{N-AFM}} = E_0 + 4J_1S^2 + 4J_2S^2 + 8J_3S^2, \quad (2)$$

$$E_{\text{S-AFM}} = E_0 - 4J_1S^2 - 4J_2S^2 + 8J_3S^2, \quad (3)$$

$$E_{\text{Z-AFM}} = E_0 + 4J_1S^2 + 4J_2S^2 - 8J_3S^2, \quad (4)$$

$$E_{\text{D-AFM}} = E_0 + 4J_1S^2 - 4J_2S^2. \quad (5)$$

As shown in Fig. 5(d), the couplings  $J_1$  and  $J_3$  are always AFM (negative sign) and  $J_2$  is FM (positive sign), depending on  $U_{\text{eff}}$ . In addition, the magnitude of the coupling strength  $J_1$  is several times higher than that of the FM coupling  $J_2$  and dozens of times higher than that of the AFM coupling  $J_3$ . In this case, the two strongest spin-exchange couplings  $J_1$  and  $J_2$  lead to alternating AFM-FM chains, which is consistent with the experimental results [52]. By changing  $U_{\text{eff}}$ , the ratio  $J_2/J_1$  increases in magnitude from  $-0.178$  to  $-0.446$ , whereas  $J_3/J_1$  increases from  $0.033$  to  $0.057$ . At  $U_{\text{eff}} = 8$  eV, the calculated strengths of the exchange couplings ( $J_2/J_1 = -0.401$  and  $J_3/J_1 = 0.052$ ) are very close to the experimental values ( $J_2/J_1 = -0.383$  and  $J_3/J_1 = 0.059$ ).

Half-filled systems usually display staggered AFM with the  $\uparrow - \downarrow - \uparrow - \downarrow$  spin structure due to the superexchange Hubbard interaction. Although the distance of FM Cu-Cu sites induced by  $J_2$  ( $\sim 2.850$  Å) is much shorter than that of the AFM  $J_1$  ( $\sim 5.806$  Å), the value of its associated magnetic coupling  $J_2$  is several times smaller than that of  $J_1$ . To understand these DFT and experimental results, we plot the Wannier functions in Fig. 6(a). It clearly shows that the effective Wannier functions of Cu's  $d_{x^2-y^2}$  display strong 1D characteristics, leading to a 1D magnetic chain system. For the interchain  $J_3$  path, the superexchange Hubbard interaction leads to an AFM coupling but with little overlap for the Cu-Cu Wannier function along the  $J_3$  path. For  $J_1$ , the magnetic coupling between two Cu sites is along the Cu-O-O-Cu path, leading to a direct overlap of Wannier functions as displayed in Fig. 6(b). For  $J_2$ , the magnetic coupling between two Cu sites is the Cu-O-Cu path, resulting in almost orthogonal overlapping Wannier functions [see Fig. 6(b)]. In this case, the  $J_1$  path, despite its longer distance, develops a stronger coupling than that over the  $J_2$  path as already explained. Based on this information from the Wannier functions, the signs of the couplings can be understood in Fig. 6(c).

For the  $J_1$  path, the Cu-O-O-Cu super-super exchange (two oxygens as the bridge) leads to an AF interaction between two  $\text{Cu}^{2+}$  spins. Considering that the Cu-O-Cu angle is close to  $90^\circ$ , the interaction becomes FM because a pair of orthogonal O  $2p$  orbitals with parallel spins are involved in the virtual electron hopping. In this case, this system forms weakly coupled alternating AFM-FM  $S = 1/2$  chains, instead of a staggered AFM chain.

Considering previous theoretical calculations for other  $\text{Cu}^{2+}$  ion materials [65–67], we also calculated the electronic structures of the D-AFM state of  $\text{Na}_2\text{Cu}_2\text{TeO}_6$  based on LSDA +  $U$  with  $U_{\text{eff}} = 8$  eV. At this  $U_{\text{eff}} = 8$  eV, the calculated magnetic couplings are  $J_1 = 23.39$ ,  $J_2 = -9.38$ , and

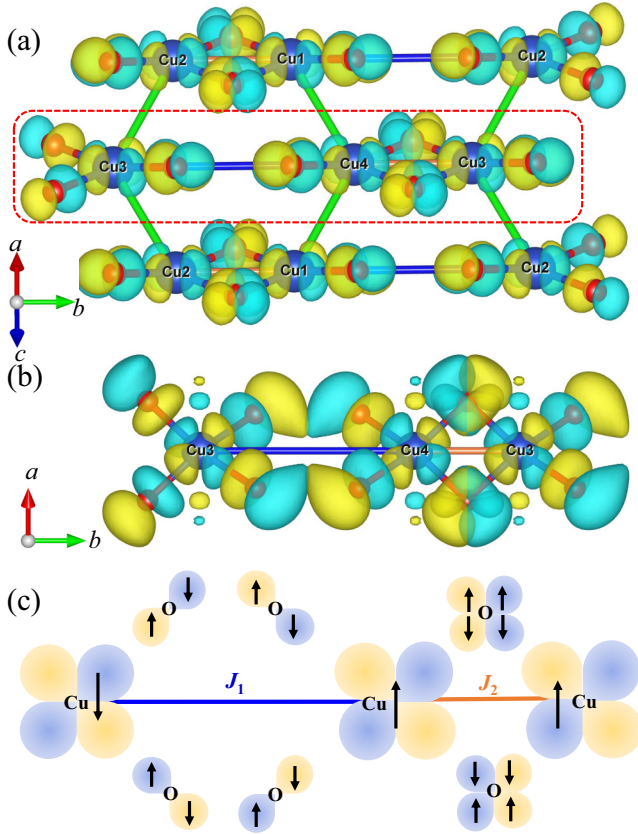


FIG. 6. (a) Side view of Wannier functions for the Cu  $3d_{x^2-y^2}$  orbital for the two-dimensional honeycomb Cu layer of  $\text{Na}_2\text{Cu}_2\text{TeO}_6$ . The isosurface is set to be 2. (b) Top view of the Wannier functions of the Cu  $3d_{x^2-y^2}$  orbital along the chain direction [red dashed rectangle part in (a)]. The isosurface is set to be 0.95. Different colors represent the  $\pm$  signs of the Wannier functions. (c) Diagrams for the super-exchange and superexchange couplings for different Cu-Cu paths along the chain direction via oxygen  $2p$  ligands. For the  $J_1$  path, the Cu-O-O-Cu super-exchange leads to the AFM alignment of the two Cu ions. For the  $J_2$  path, Cu-O-Cu superexchange with a bonding angle of  $90^\circ$  results in a FM exchange between the nearest-neighbor two ions. Note, we presented a similar figure in Ref. [52] but have included this information here for ease of reference.

$J_3 = 1.22$  meV, which are in good agreement with the values obtained from neutron experiments ( $J_1 = 22.78$ ,  $J_2 = -8.73$ , and  $J_3 = 1.34$  meV) [52].

Because the particular value of  $U_{\text{eff}}$  would affect the electronic structure of  $\text{Na}_2\text{Cu}_2\text{TeO}_6$ , we also estimated the  $U_{\text{eff}}$  parameter from the Cu  $d$  electrons by using the linear response approximation [68]. As shown in Fig. 7(a) for a  $1 \times 2 \times 1$  supercell, the NSCF and SCF slopes are 0.24133 and 0.08433, respectively. Then according to linear-response equation [68], we obtain

$$U_{\text{eff}} = \chi_0^{-1} - \chi^{-1} \approx \left( \frac{\partial N_d^{\text{SCF}}}{\partial V} \right)^{-1} - \left( \frac{\partial N_d^{\text{NSCF}}}{\partial V} \right)^{-1} \\ = \left( \frac{1}{0.08433} - \frac{1}{0.24133} \right) \text{eV} \approx 7.71 \text{ eV}.$$

Furthermore, we also calculated the  $U_{\text{eff}}$  coupling by considering different supercells, leading to similar values for  $U_{\text{eff}}$

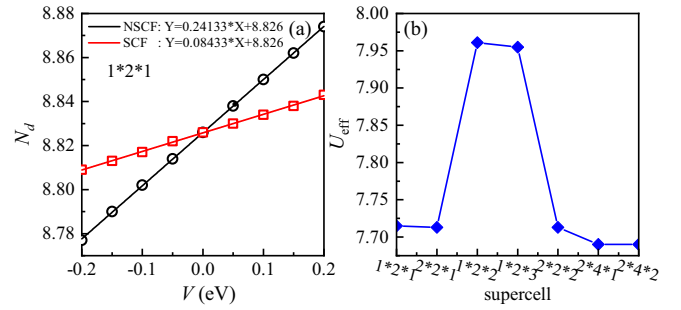


FIG. 7. (a) The non-self-consistent (NSCF) and self-consistent (SCF) response functions from linear regression of the relationship between the number of  $d$  electrons that result from a range of rigid potential shifts  $V$ . Here  $1 \times 2 \times 1$  supercell is taken as an example. (b) The calculated  $U_{\text{eff}}$  parameter vs different supercells.

(in the range of 7.69–7.96 eV) as displayed in Fig. 7(b). These values are close to  $U_{\text{eff}} = 8$  eV. As a consequence, the value  $U_{\text{eff}} = 8$  eV is reasonable to be used in the following calculations of electronic structures.

As displayed in Fig. 8(a), the Cu  $3d$  orbitals shift away from the Fermi level whereas the O  $2p$  states are close to that Fermi level, supporting the charge-transfer picture. Figures 8(b) and 8(c) indicate that the half-occupied  $d_{x^2-y^2}$  orbitals display strong Mott-insulating behavior, whereas other Cu's  $3d$  orbitals are fully occupied. In this case, this system is locally in a total  $S = 1/2$  state where the magnetism is contributed by the  $d_{x^2-y^2}$  state. Note that this effective  $U_{\text{eff}}$  employed in the DFT calculations is different from the Hubbard  $U$  in our DMRG calculations. As shown in Fig. 8, the gap of the  $d_{x^2-y^2}$  orbital is about  $\sim 10$  eV at  $U_{\text{eff}} = 8$  eV in DFT calculations, corresponding to the Mott gap ( $\sim U - 2W$ ) induced by the Hubbard  $U$  in the Hubbard model. Furthermore, for the Cu-O-O-Cu  $J_1$  path in  $\text{Na}_2\text{Cu}_2\text{TeO}_6$ , we also found a small net magnetization at the oxygens of  $0.05\mu_B$ , which originates from the hybridization between atoms and mobility of the electrons as discussed in Ref. [69].

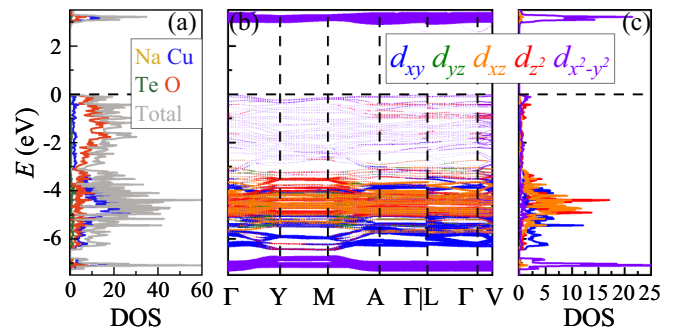


FIG. 8. (a) DOS near the Fermi level of  $\text{Na}_2\text{Cu}_2\text{TeO}_6$  for the D-AFM phase (Gray: total; yellow: Na; blue: Cu; dark cyan: Te; red: O). (b) Projected band structures and (c) DOS of the D-AFM phase for  $\text{Na}_2\text{Cu}_2\text{TeO}_6$ , respectively. Note that the local  $\{x, y, z\}$  axes of projected orbitals are marked in Fig. 1(a). The weight of each Cu orbital is represented by the size of the circles in the projected band structures.

#### IV. SINGLE-ORBITAL HUBBARD MODEL METHOD

A wide variety of real materials also have dominant 1D-like physical properties, even without restrictive 1D geometries in their crystal structure. For those systems, interesting phenomena caused by strongly anisotropic electronic structures have been qualitatively unveiled in theory by using simple 1D models, including 1D spin order [5,52], ferroelectronic distortion [25,70], orbital ordering [71,72], nodes in the spin density [69], as well as dimerization [27,73,74].

To better understand the magnetic coupling for the dimer chain direction, an effective single-orbital Hubbard model was constructed to calculate the real-space spin correlations via the density-matrix renormalization-group method [75–78] where we have used the DMRG++ software [79]. The model studied here includes the kinetic energy and interaction energy terms  $H = H_k + H_{int}$ ,

$$H = \sum_{i,\sigma,\alpha} t_\beta (c_{i\sigma}^\dagger c_{i+\alpha,\sigma} + \text{H.c.}) + U \sum_i n_{i\uparrow} n_{i\downarrow}, \quad (6)$$

where the first term represents the hopping of an electron from site  $i$  to site  $i + \alpha$ . The number  $\beta$  indicates the three different hoppings ( $t_1$ ,  $t_2$ , and  $t_4$ ) as shown in Fig. 3(c). The second term is the standard intraorbital Hubbard repulsion.

Here, we employed a  $L = 36$ -sites chain with open-boundary conditions. Furthermore, at least, 3000 states were kept and up to 17 finite loop sweeps were performed during our DMRG calculations. We also tested other different sizes, such as  $L = 16, 24, 40$  sites, and the results are robust. The electronic filling  $n = 1$  in the active one orbital is considered. This electronic density (one electron in one orbital) corresponds to the total  $S = 1/2$  configuration of the  $d^9$  configuration of  $\text{Cu}^{2+}$ . In the tight-binding term, we only considered three hoppings:  $t_1 = 0.178$ ,  $t_2 = 0.012$ , and  $t_4 = 0.017$  (in eV).

#### V. DMRG RESULTS

##### A. Magnetic properties

The distorted honeycomb crystal structure studied here is characterized as a low-dimensional spin system due to strong quantum fluctuations [47,48,53]. Because DFT neglects fluctuations, here we adopted the advanced many-body DMRG method to discuss the quantum magnetic coupling in this  $S = 1/2$  dimerized chain system. To understand the magnetic coupling along the dimerized chain, we measured the real-space spin-spin correlations  $\langle \mathbf{S}_i \cdot \mathbf{S}_j \rangle$ . Here the spin at site  $i$  is

$$\mathbf{S}_i = \frac{1}{2} \sum_\gamma \sum_{\alpha\beta} c_{i\gamma\alpha}^\dagger \boldsymbol{\sigma}_{\alpha\beta} c_{i\gamma\beta}, \quad (7)$$

where  $\boldsymbol{\sigma}_{\alpha\beta}$  are the matrix elements of the Pauli matrices.

Figure 9 shows the spin-spin correlation  $\langle \mathbf{S}_i \cdot \mathbf{S}_j \rangle$  vs site index for different values of  $U$  and length  $L$ . The distance is  $r = |i - j|$  with  $i$  and  $j$  site indices. The spin-spin correlation decays very fast with distance  $r$ , suggesting a long-range disordered phase in this dimerized chain because it is composed of strong dimer spin-singlet states  $[(|\uparrow\downarrow\rangle - |\downarrow\uparrow\rangle)/\sqrt{2}]$ , nearly decoupled from one another. As shown in the inset of Figs. 9(a) and 9(b), the correlation between dimers is FM but

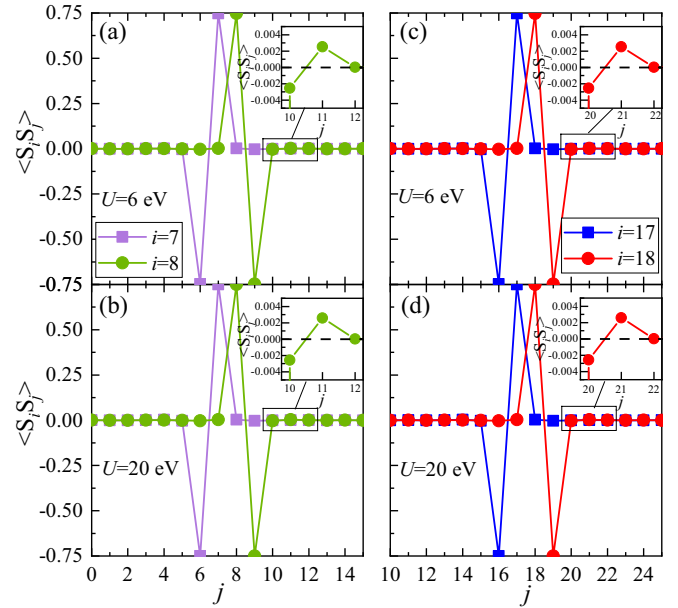


FIG. 9. (a) and (b) Spin-spin correlations  $\langle \mathbf{S}_i \cdot \mathbf{S}_j \rangle$  in real space for (a)  $U = 6$  eV and (b)  $U = 20$  eV, using  $L = 16$ . (c) and (d) Spin-spin correlations  $\langle \mathbf{S}_i \cdot \mathbf{S}_j \rangle$  in real space for (c)  $U = 6$  eV and (d)  $U = 20$  eV, using  $L = 36$ . The insets: the FM correlation between dimers is shown.

weak for  $L = 16$ . Furthermore, we also studied the  $L = 36$  case. These results are similar to the results of  $L = 16$ , indicating that our conclusions of spin-singlet state, nearly decoupled from one another with weak FM, are robust against changes in  $L$ .

In the range of  $U/W$  studied here, we observed a robust AFM-FM correlation along the chain direction. This AFM-FM correlation chain is reasonable. The magnetic coupling in a dimer should be AFM because the large overlap of  $\text{Cu-}3d_{x^2-y^2}$  orbitals establishes AFM coupling in a dimer according to the Cu-O-O-Cu super-super-exchange ideas, mediated by  $t_1$ . Between neighboring Cu-Cu dimers, our DMRG calculations predict a short-range weaker FM correlation, which is actually mediated by  $t_4$ .

##### B. Binding energy

Considering that superconductivity was widely reported in doped Cu-based compounds with the  $d^9$  electronic configuration [2], we also studied the case of hole doping in  $\text{Na}_2\text{Cu}_2\text{TeO}_6$ . To explore possible pairing tendencies, we studied the binding energy of a pair of holes defined as [2]

$$\Delta E = E(N - 2) + E(N) - 2E(N - 1), \quad (8)$$

where  $E(N)$  is the ground-state energy of the undoped case with half-filling for the single-orbital chain model.  $E(N - 2)$  and  $E(N - 1)$  are the ground-state energies of the two-hole doped or one-hole doped cases. Here,  $\Delta E$  is negative, indicating pairing tendencies because the particles minimize their energy by creating a bound state. However, if the holes become two independent particles, this corresponds to zero binding energy in the bulk limit. In the case where the particles

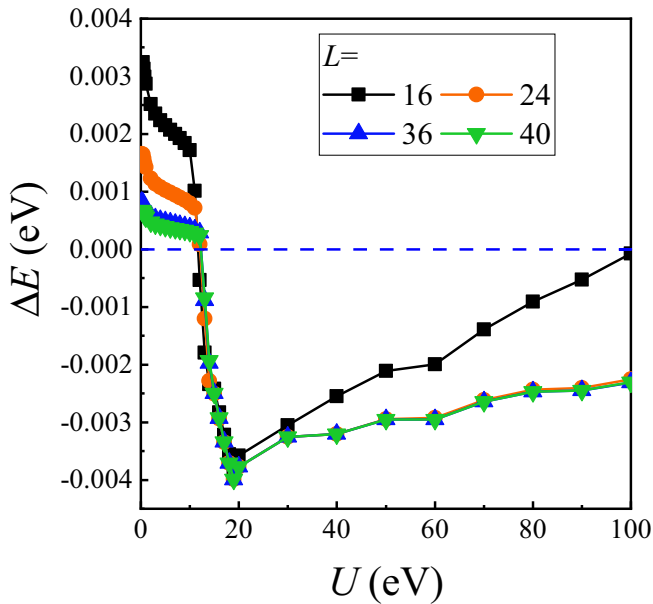


FIG. 10. Binding energy vs  $U$  calculated with DMRG for different chain lengths  $L$ . In all cases shown, we observed the possible pairing tendencies in the strong Hubbard  $U$  region. The minimum of the binding energy (strongest binding tendency) can be found at  $U \sim 20$  eV in all cases.

do not bind, this quantity is positive for finite systems and should converge to zero as the size of the cluster increases.

Based on the calculated ground-state energies for the cases  $N$ ,  $N - 1$  (one hole), and  $N - 2$  (two holes), we obtain the binding energy  $\Delta E$  for different chain lengths  $L$  as shown in Fig. 10. The results clearly show that the binding energy  $\Delta E$  becomes negative in the region Hubbard  $U \sim 11$  eV and larger, displaying a broad binding region in Fig. 10. In addition, the minimum of the binding energy  $\Delta E$  is found at about  $U \sim 20$  eV. Here, the absolute value of binding energy  $|\Delta E|$  is quite small due to the very tiny hopping  $t_2$  between singlet dimers.

To better understand the pairing implication of the negative binding energy obtained from Fig. 10, we have also calculated the real-space distribution of charge density in the doped system.

Figure 11(a) shows the electronic density  $n$  of the  $N - 2$  case for different Hubbard interactions  $U$ . In the small  $U$  region, the electronic density  $n$  indicates that the hole density ( $1 - n$ ) wants to spread apart. In this case, as a consequence, no pairing in this region  $U \leq 10$  eV was found. However, as  $U$  increases, the hole density of the pair of holes (the minima) get closer, suggesting that holes prefer to be together, corresponding to the region of negative binding energy. It is also shown that at  $U = 20$  eV the holes are closer than at other values of  $U$ . Qualitatively, this kind of results resemble the binding energy because there is more binding at  $U = 20$  eV than at other  $U$ 's.

In addition, we also studied the real-space electronic density  $n$  for different hole-doping cases at  $U = 20$  eV [see Fig. 11(b)]. For  $N$  electrons, corresponding to the half-filled orbital, the electronic density is uniform at  $n = 1$  for different

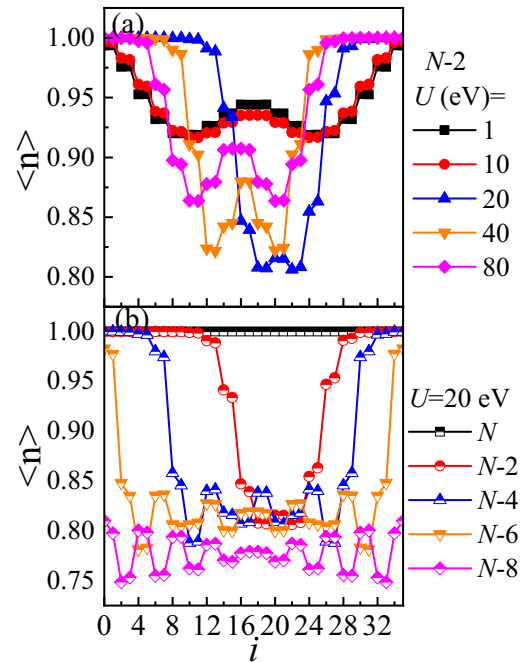


FIG. 11. (a) Real-space electronic density  $n$  of the  $N - 2$  case for different Hubbard interactions  $U$ . (b) Real-space electronic density  $n$  for different hole-doping cases at  $U = 20$  eV. Here, we used a chain length  $L = 36$ .

sites  $i$ . In the case of  $N - 2$  electrons, i.e., two holes, these two holes are located near the center of the cluster, in a tight manner compatible with the small pairing.

## VI. LANCZOS RESULTS

We also performed Lanczos studies on a 16-site cluster, complementary to our DMRG results. In Fig. 12, we show the binding energy ( $\Delta E$ ) vs the interaction strength  $U$ . First, consistent with our DMRG results the binding energy behaves quite similarly with the maximum binding happening at  $U \sim$

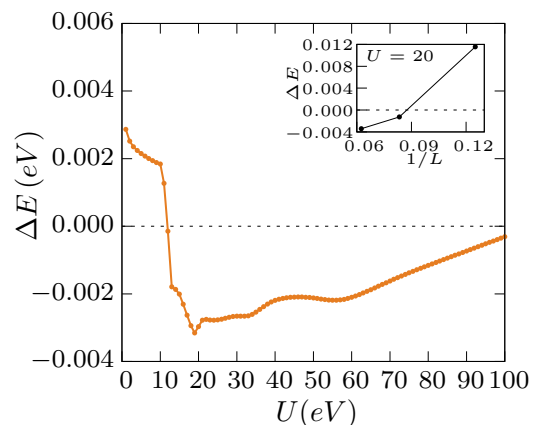


FIG. 12. Binding energy  $\Delta E$  vs  $U$  for a 16-site cluster via Lanczos. The inset shows the growth of binding as we increase the system size at  $U = 20$  (in eV). For the inset plot, system sizes  $L = 8, 12,$  and  $16$  were considered.

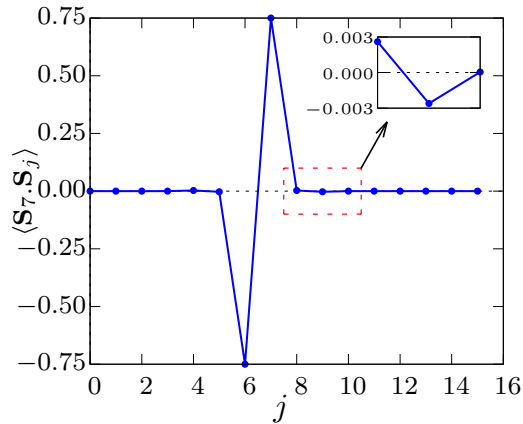


FIG. 13. Real-space spin-spin correlations with respect to site 7 at  $U = 20$  for a 16-site cluster via Lanczos.

20 eV. Second, the figure in the inset shows the robustness of the binding energy at  $U = 20$  eV as we increase the system size (points shown are for  $L = 8, 12,$  and  $16$  sites). This is an important observation since computationally only small lattice sizes can be studied via Lanczos, and even within this limitation we observe  $\Delta E$  becoming more negative as we increase the system sizes. Note that for all these Lanczos results the maximum convergence error is on the order of  $10^{-8}$ .

Similar to our DMRG study in the previous section, we have computed the real-space spin-spin correlation for a 16-site chain via Lanczos, see Fig. 13. We observed that our results are in good agreement with DMRG results, providing further confirmation to our study.

## VII. CONCLUSIONS

In this paper, we have systematically studied the dimerized chain system  $\text{Na}_2\text{Cu}_2\text{TeO}_6$  by combining first-principles DFT as well as DMRG and Lanczos calculations. Based on the *ab initio* DFT calculations for the nonmagnetic state, we found that the states near the Fermi level are mainly contributed by the Cu  $3d$  states highly hybridized with the O  $2p$  orbitals, leading to an effective one-orbital low-energy model. Furthermore, we obtained three magnetic exchange interactions ( $J_1$ ,  $J_2$ , and  $J_3$ ) by mapping the DFT energies to a Heisenberg model. In this case,  $J_1$  and  $J_3$  are AFM couplings and  $J_2$  is FM, in agreement with experimental results. Based on the

Wannier functions from first-principles calculations, we obtained the relevant hopping amplitudes and an effective  $d_{x^2-y^2}$  Wannier function in combination with O  $2p$  states, leading to a spin-singlet formation in an AFM dimer. In this AFM dimer, the strong Cu-O-O-Cu super-super exchange plays the main role in generating the largest AFM coupling between the long-distanced Cu-Cu sites due to the direct overlapping of the effective Wannier functions (combination of Cu  $3d_{x^2-y^2}$  and O  $2p$  states). Furthermore, the exchange interaction of the  $J_2$  path is FM because the Cu-O-Cu angle is close to  $90^\circ$ , i.e., a pair of orthogonal O  $2p$  orbitals with parallel spins are involved in the virtual electron hopping.

In addition, we constructed a single-orbital Hubbard model for this dimerized chain system where the quantum fluctuations are taken into account. The AFM-FM magnetic coupling ( $\uparrow - \downarrow - \downarrow - \uparrow$ ) along the chain was found in our DMRG calculations, in agreement with DFT calculations and neutron-scattering results. Furthermore, we also calculated the binding energy  $\Delta E$  and observed that it becomes negative starting at approximately Hubbard  $U \sim 11$  eV and beyond, indicating possible pairing tendencies, forming very small-size Cooper pairs. Furthermore, we also studied several hole-doping cases, still suggesting that the pairing tendency is robust. Because the hole pairs are so tight, likely the critical temperature related to this material will be very small. Namely, we are in a Bose-Einstein condensate regime, assuming these tight pairs can form a coherent superconducting state. Overall, our results for  $\text{Na}_2\text{Cu}_2\text{TeO}_6$ —including short-range magnetic couplings, doping effects, and possible pairing tendencies—provide guidance to experimentalists and theorists working on this dimerized chain system.

## ACKNOWLEDGMENTS

The work of L.-F.L., R.S., Y.Z., S.G., A.M, A.D.C., M.B.S., and E.D. was supported by the U.S. Department of Energy (DOE), Office of Science, Basic Energy Sciences (BES), Materials Sciences and Engineering Division. G.A. was partially supported by the Scientific Discovery through Advanced Computing (SciDAC) Program funded by the U.S. DOE, Office of Science, Advanced Scientific Computing Research and BES, Division of Materials Sciences and Engineering. M.B.S. is supported by the Scientific User Facilities Division, Office of Basic Energy Sciences, US DOE, under Contract No. DE-AC0500OR22725 with UT Battelle, LLC.

- [1] B. Bertini, F. Heidrich-Meisner, C. Karrasch, T. Prosen, R. Steinigeweg, and M. Žnidarič, *Rev. Mod. Phys.* **93**, 025003 (2021).
- [2] E. Dagotto, *Rev. Mod. Phys.* **66**, 763 (1994).
- [3] M. Grioni, S. Pons, and E. Frantzeskakis, *J. Phys.: Condens. Matter* **21**, 023201 (2008).
- [4] E. Dagotto, *Rev. Mod. Phys.* **85**, 849 (2013).
- [5] L.-F. Lin, Y. Zhang, G. Alvarez, A. Moreo, and E. Dagotto, *Phys. Rev. Lett.* **127**, 077204 (2021).
- [6] E. Dagotto and T. M. Rice, *Science* **271**, 618 (1996).
- [7] E. Dagotto, *Rep. Prog. Phys.* **62**, 1525 (1999).
- [8] M. Uehara, T. Nagata, J. Akimitsu, H. Takahashi, N. Môri, and K. Kinoshita, *J. Phys. Soc. Jpn.* **65**, 2764 (1996).

- [9] H. Takahashi, A. Sugimoto, Y. Nambu, T. Yamauchi, Y. Hirata, T. Kawakami, M. Avdeev, K. Matsubayashi, F. Du, C. Kawashima, H. Soeda, S. Nakano, Y. Uwatoko, Y. Ueda, T. J. Sato, and K. Ohgushi, *Nature Mater.* **14**, 1008 (2015).
- [10] J. Ying, H. Lei, C. Petrovic, Y. Xiao, and V. V. Struzhkin, *Phys. Rev. B* **95**, 241109(R) (2017).
- [11] Y. Zhang, L. F. Lin, J. J. Zhang, E. Dagotto, and S. Dong, *Phys. Rev. B* **95**, 115154 (2017).
- [12] Y. Zhang, L.-F. Lin, J.-J. Zhang, E. Dagotto, and S. Dong, *Phys. Rev. B* **97**, 045119 (2018).
- [13] Y. Zhang, L.-F. Lin, A. Moreo, S. Dong, and E. Dagotto, *Phys. Rev. B* **100**, 184419 (2019).

- [14] Y. Zhang, L.-F. Lin, A. Moreo, S. Dong, and E. Dagotto, *Phys. Rev. B* **101**, 144417 (2020).
- [15] J. Rincón, A. Moreo, G. Alvarez, and E. Dagotto, *Phys. Rev. Lett.* **112**, 106405 (2014).
- [16] Y. Zhang, L.-F. Lin, G. Alvarez, A. Moreo, and E. Dagotto, *Phys. Rev. B* **104**, 125122 (2021).
- [17] L.-F. Lin, Y. Zhang, G. Alvarez, J. Herbrych, A. Moreo, and E. Dagotto, *Phys. Rev. B* **105**, 075119 (2022).
- [18] J. Herbrych, J. Heverhagen, G. Alvarez, M. Daghofer, A. Moreo, and E. Dagotto, *Proc. Natl. Acad. Sci. USA* **117**, 16226 (2020).
- [19] B. Pandey, L.-F. Lin, R. Soni, N. Kaushal, J. Herbrych, G. Alvarez, and E. Dagotto, *Phys. Rev. B* **102**, 035149 (2020).
- [20] J. Herbrych, G. Alvarez, A. Moreo, and E. Dagotto, *Phys. Rev. B* **102**, 115134 (2020).
- [21] B. Pandey, R. Soni, L.-F. Lin, G. Alvarez, and E. Dagotto, *Phys. Rev. B* **103**, 214513 (2021).
- [22] M. Środa, E. Dagotto, and J. Herbrych, *Phys. Rev. B* **104**, 045128 (2021).
- [23] N. Kaushal, R. Soni, A. Nocera, G. Alvarez, and E. Dagotto, *Phys. Rev. B* **101**, 245147 (2020).
- [24] N. Kaushal, J. Herbrych, G. Alvarez, and E. Dagotto, *Phys. Rev. B* **104**, 235135 (2021).
- [25] L.-F. Lin, Y. Zhang, A. Moreo, E. Dagotto, and S. Dong, *Phys. Rev. Mater.* **3**, 111401(R) (2019).
- [26] J. Gooth, B. Bradlyn, S. Honnali, C. Schindler, N. Kumar, J. Noky, Y. Qi, C. Shekhar, Y. Sun, Z. Wang, B. A. Bernevig, and C. Felser, *Nature (London)* **575**, 315 (2019).
- [27] Y. Zhang, L.-F. Lin, A. Moreo, S. Dong, and E. Dagotto, *Phys. Rev. B* **101**, 174106 (2020).
- [28] N. D. Patel, N. Kaushal, A. Nocera, G. Alvarez, and E. Dagotto, *npj Quantum Mater.* **5**, 27 (2020).
- [29] J. Herbrych, M. Środa, G. Alvarez, M. Mierzejewski, and E. Dagotto, *Nat. Commun.* **12**, 2955 (2021).
- [30] T. Hotta and E. Dagotto, *Phys. Rev. Lett.* **88**, 017201 (2001).
- [31] J. Riera, K. Hallberg, and E. Dagotto, *Phys. Rev. Lett.* **79**, 713 (1997).
- [32] Y. Zhang, L.-F. Lin, A. Moreo, and E. Dagotto, *Appl. Phys. Lett.* **120**, 023101 (2022).
- [33] K. Hida, *Phys. Rev. B* **46**, 8268 (1992).
- [34] K. Hida, *J. Phys. Soc. Jpn.* **63**, 2514 (1994).
- [35] I. Affleck, *J. Phys.: Condens. Matter* **1**, 3047 (1989).
- [36] G. S. Uhrig and H. J. Schulz, *Phys. Rev. B* **54**, R9624 (1996).
- [37] F. D. M. Haldane, *Phys. Rev. Lett.* **50**, 1153 (1983).
- [38] I. Affleck, T. Kennedy, E. H. Lieb, and H. Tasaki, *Phys. Rev. Lett.* **59**, 799 (1987).
- [39] K. Hida, *Phys. Rev. B* **45**, 2207 (1992).
- [40] M. Kohmoto and H. Tasaki, *Phys. Rev. B* **46**, 3486 (1992).
- [41] F. Pollmann, A. M. Turner, E. Berg, and M. Oshikawa, *Phys. Rev. B* **81**, 064439 (2010).
- [42] A. Miyake, *Phys. Rev. Lett.* **105**, 040501 (2010).
- [43] K. Kodama, H. Harashina, H. Sasaki, M. Kato, M. Sato, K. Kakurai, and M. Nishi, *J. Phys. Soc. Jpn.* **68**, 237 (1999).
- [44] M. B. Stone, W. Tian, M. D. Lumsden, G. E. Granroth, D. Mandrus, J.-H. Chung, N. Harrison, and S. E. Nagler, *Phys. Rev. Lett.* **99**, 087204 (2007).
- [45] Y. Miura, Y. Yasui, T. Moyoshi, M. Sato, and K. Kakurai, *J. Phys. Soc. Jpn.* **77**, 104709 (2008).
- [46] E. S. Klyushina, A. T. M. N. Islam, J. T. Park, E. A. Goremychkin, E. Wheeler, B. Klemke, and B. Lake, *Phys. Rev. B* **98**, 104413 (2018).
- [47] J. Xu, A. Assoud, N. Soheilnia, S. Derakhshan, H. L. Cuthbert, J. E. Greedan, M. H. Whangbo, and H. Kleinke, *Inorg. Chem.* **44**, 5042 (2005).
- [48] Y. Miura, R. Hirai, Y. Kobayashi, and M. Sato, *J. Phys. Soc. Jpn.* **75**, 084707 (2006).
- [49] S. Derakhshan, H. L. Cuthbert, J. E. Greedan, B. Rahaman, and T. Saha-Dasgupta, *Phys. Rev. B* **76**, 104403 (2007).
- [50] H.-J. Koo and M.-H. Whangbo, *Inorg. Chem.* **47**, 128 (2008).
- [51] M. Schmitt, O. Janson, S. Golbs, M. Schmidt, W. Schnelle, J. Richter, and H. Rosner, *Phys. Rev. B* **89**, 174403 (2014).
- [52] S. Gao, L.-F. Lin, A. F. May, B. K. Rai, Q. Zhang, E. Dagotto, A. D. Christianson, and M. B. Stone, *Phys. Rev. B* **102**, 220402(R) (2020).
- [53] Y. Shangguan, S. Bao, Z.-Y. Dong, Z. Cai, W. Wang, Z. Huang, Z. Ma, J. Liao, X. Zhao, R. Kajimoto, K. Iida, D. Voneshen, S.-L. Yu, J.-X. Li, and J. Wen, *Phys. Rev. B* **104**, 224430 (2021).
- [54] G. Kresse and J. Furthmüller, *Phys. Rev. B* **54**, 11169 (1996).
- [55] G. Kresse and D. Joubert, *Phys. Rev. B* **59**, 1758 (1999).
- [56] P. E. Blöchl, *Phys. Rev. B* **50**, 17953 (1994).
- [57] J. P. Perdew, K. Burke, and M. Ernzerhof, *Phys. Rev. Lett.* **77**, 3865 (1996).
- [58] J. P. Perdew, A. Ruzsinszky, G. I. Csonka, O. A. Vydrov, G. E. Scuseria, L. A. Constantin, X. Zhou, and K. Burke, *Phys. Rev. Lett.* **100**, 136406 (2008).
- [59] A. I. Liechtenstein, V. I. Anisimov, and J. Zaanen, *Phys. Rev. B* **52**, R5467 (1995).
- [60] N. Marzari and D. Vanderbilt, *Phys. Rev. B* **56**, 12847 (1997).
- [61] A. A. Mostofi, J. R. Yates, Y.-S. Lee, I. Souza, D. Vanderbilt, and N. Marzari, *Comput. Phys. Commun.* **178**, 685 (2008).
- [62] K. Momma and F. Izumi, *J. Appl. Crystallogr.* **44**, 1272 (2011).
- [63] Y. Zhang, L.-F. Lin, W. Hu, A. Moreo, S. Dong, and E. Dagotto, *Phys. Rev. B* **102**, 195117 (2020).
- [64] S. L. Dudarev, G. A. Botton, S. Y. Savrasov, C. J. Humphreys, and A. P. Sutton, *Phys. Rev. B* **57**, 1505 (1998).
- [65] T. C. Sterling and D. Reznik, *Phys. Rev. B* **104**, 134311 (2021).
- [66] N. Pavlenko, I. Elfimov, T. Kopp, and G. A. Sawatzky, *Phys. Rev. B* **75**, 140512(R) (2007).
- [67] K.-W. Lee and W. E. Pickett, *Phys. Rev. B* **70**, 165109 (2004).
- [68] M. Cococcioni and S. de Gironcoli, *Phys. Rev. B* **71**, 035105 (2005).
- [69] L.-F. Lin, N. Kaushal, C. Sen, A. D. Christianson, A. Moreo, and E. Dagotto, *Phys. Rev. B* **103**, 184414 (2021).
- [70] L.-F. Lin, Q.-R. Xu, Y. Zhang, J.-J. Zhang, Y.-P. Liang, and S. Dong, *Phys. Rev. Mater.* **1**, 071401(R) (2017).
- [71] B. Pandey, Y. Zhang, N. Kaushal, R. Soni, L.-F. Lin, W.-J. Hu, G. Alvarez, and E. Dagotto, *Phys. Rev. B* **103**, 045115 (2021).
- [72] L.-F. Lin, N. Kaushal, Y. Zhang, A. Moreo, and E. Dagotto, *Phys. Rev. Mater.* **5**, 025001 (2021).
- [73] Y. Zhang, L.-F. Lin, A. Moreo, G. Alvarez, and E. Dagotto, *Phys. Rev. B* **103**, L121114 (2021).
- [74] Y. Zhang, L.-F. Lin, A. Moreo, and E. Dagotto, *Phys. Rev. B* **104**, L060102 (2021).
- [75] S. R. White, *Phys. Rev. Lett.* **69**, 2863 (1992).
- [76] S. R. White, *Phys. Rev. B* **48**, 10345 (1993).
- [77] U. Schollwöck, *Rev. Mod. Phys.* **77**, 259 (2005).
- [78] K. A. Hallberg, *Adv. Phys.* **55**, 477 (2006).
- [79] G. Alvarez, *Comput. Phys. Commun.* **180**, 1572 (2009).